ANALYTICAL AND EXPERIMENTAL LATERAL LOAD BEHAVIOR OF UNBONDED POST-TENSIONED PRECAST CONCRETE WALLS

Felipe J. Perez, Ph.D., P.E., Civil Engineering Department, Cal Poly Pomona, CA
Richard Sause, Ph.D., P.E., Dept. of Civil and Env. Engineering, Lehigh University, PA
Stephen Pessiki, Ph.D., Dept. of Civil and Env. Engineering, Lehigh University, PA

ABSTRACT

This study analytically and experimentally evaluates the response of unbonded post-tensioned precast concrete walls with horizontal joints (UPT walls) under combined gravity and lateral loads. A design-oriented analytical model is introduced, which uses simple formulae to estimate the nonlinear lateral load behavior of UPT walls. This simple model is compared with experimental results. A previously developed UPT wall model based on fiber elements is also compared with experimental results. Each model is formulated to consider several critical limit states in the lateral load behavior of UPT walls.

Comparisons show good agreement between analytical and experimental results for five different test walls under monotonic and cyclic loading. The simple model is found to be sufficiently accurate for seismic design of UPT walls. The accuracy of the fiber model in predicting the cyclic lateral load response of the walls depends on the amount of initial prestress on the walls. In general, the accuracy of the fiber model is good, but caution must be exercised when analyzing lightly prestressed UPT walls under cyclic or dynamic loading using the fiber model, because the base shear capacity may be overestimated.

Keywords: Concrete, Post-tensioned, Precast, Seismic, Unbonded, Walls.

INTRODUCTION

The use of unbonded post-tensioned precast concrete walls with horizontal joints (UPT walls) as the primary lateral load resisting system in seismic zones has been studied previously. Analytical work has investigated the performance of these walls under earthquake loading[1]. Seismic design studies have shown the influence of design parameters and outlined performance-based design objectives and criteria[2,3]. Limited experimental results[4,5,6,7] have demonstrated the excellent performance of UPT walls as a seismic-resistant structural system.

This paper introduces a design-oriented analytical model that uses relatively simple formulae to estimate the nonlinear lateral load behavior of UPT walls. Results from this simple model and from a fiber model developed by Kurama et al.[2] are compared with available experimental results.

EXPECTED LATERAL LOAD BEHAVIOR

The full-scale- and reduced-scale prototype UPT walls considered in the present study are shown schematically in Fig. 1. The reduced-scale wall is obtained by scaling the full-scale prototype wall by a factor of 5/12, except for the thickness which is scaled by a factor of 1/2 so that the wall cross-section can accommodate the reinforcing steel and cover concrete. The walls are comprised of six one-story-tall precast panels that are connected along horizontal joints using unbonded post-tensioning (PT) steel, which is anchored at the roof and at the base. Each wall has special confining reinforcement at the ends of the base panel so that it can sustain the large compressive strains that develop there.

Two different reinforcement details are considered in the base panel of the reduced-scale wall as shown in Fig. 1(d) because one wall tested with spiral confinement suffered an unexpected buckling failure in the base panel which was subsequently mitigated by modifying the reinforcement details using hoop confinement.

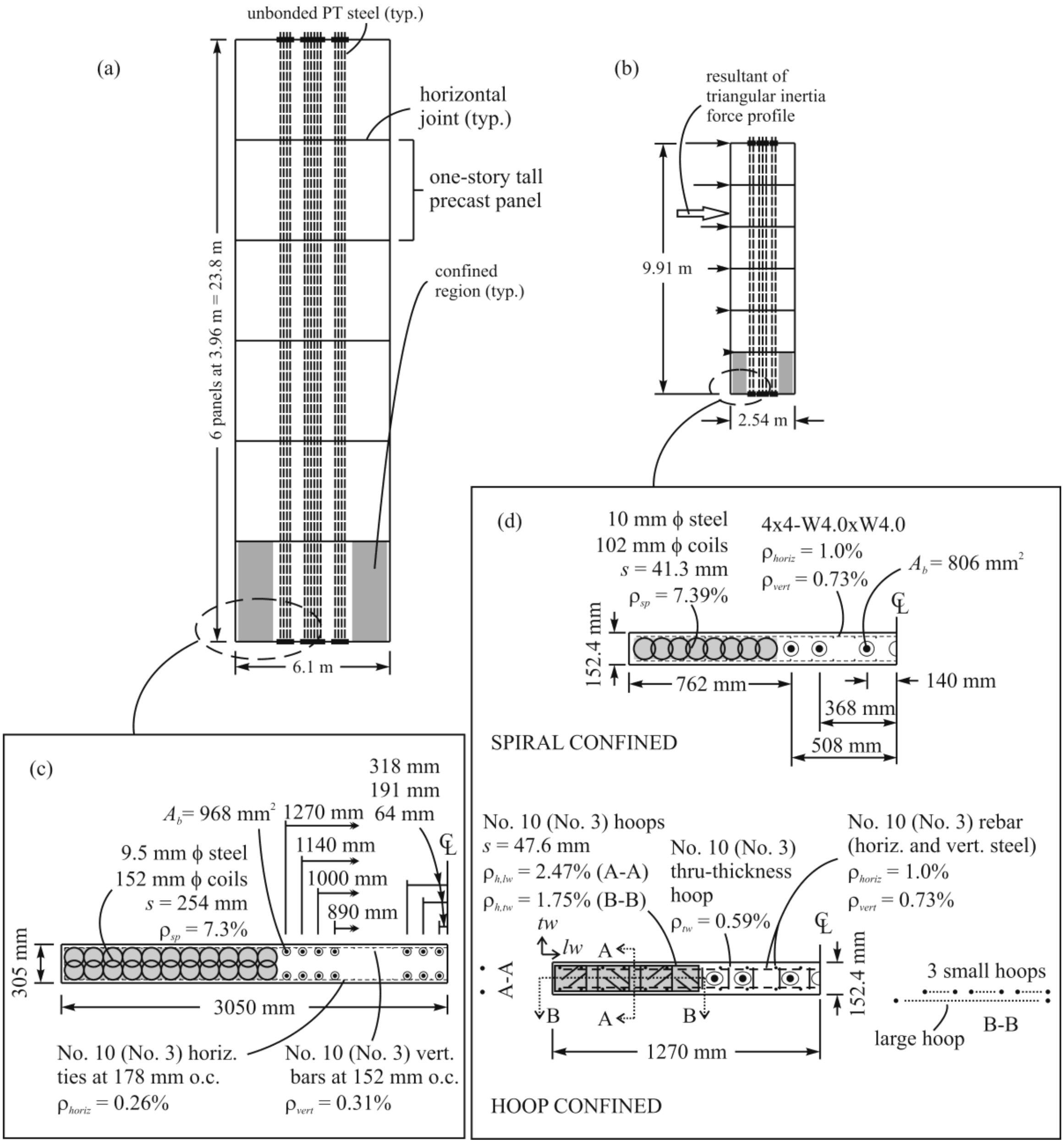

Fig.1 Full-scale and reduced-scale UPT walls.

The lateral load behavior of a well-designed UPT wall should be controlled by flexural behavior rather than by shear sliding at the base. Assuming that flexural (overturning) behavior controls, the lateral load behavior of UPT walls is characterized by the limit states shown in Fig. 2: (1) decompression at the wall base (DEC), denoted by the symbol (■); (2) effective linear limit of response (ELL), denoted by the symbol (○); (3) initiation of cover spalling (SPL), denoted by the symbol (◊); (4) yielding of the PT steel (LLP), denoted by the symbol (□); (5) base shear capacity, denoted by the symbol (•); (6) loss of prestress under cyclic lateral load (not shown in Fig. 2); and (7) crushing of confined concrete (CCC), denoted by the symbol (▲). The limit states are described below. Limit states (2) ELL, (4) LLP, and (6) CCC define a tri-linear idealization of the wall response, which is the basis for the simple analytical model described in the next section.

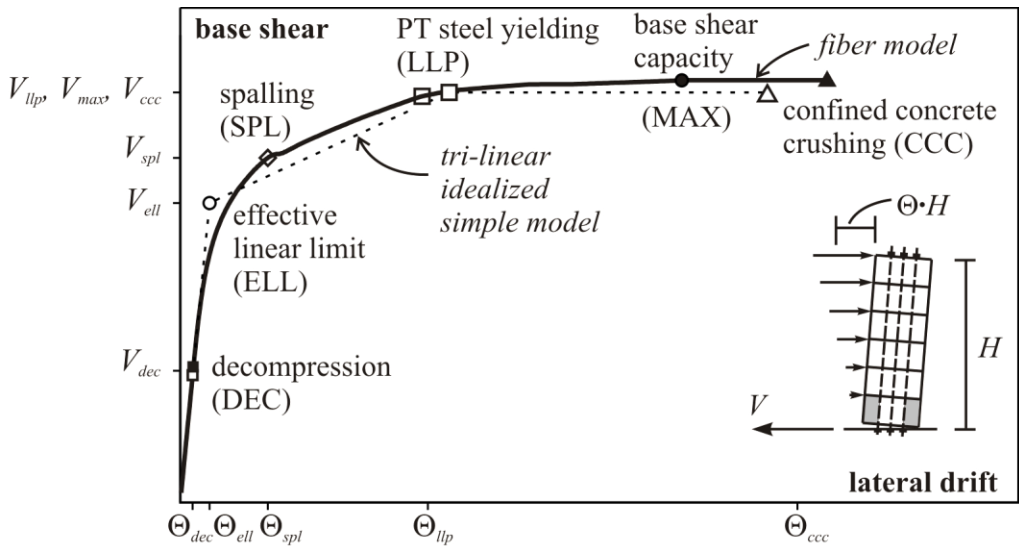

Fig. 2 Expected lateral load behavior of UPT walls

DECOMPRESSION

Decompression at the wall base occurs when the precompression due to post-tensioning and gravity loads is reduced to zero at one end of the wall base by the overturning moment due to lateral loads. Under a specified lateral load distribution, decompression of the wall can be related to a specific level of base shear and lateral drift, V_{dec} and Θ_{dec} respectively. Decompression is accompanied by the initiation of gap opening along the base joint of the wall.

EFFECTIVE LINEAR LIMIT

The lateral load response of a UPT precast concrete wall is essentially linear elastic immediately after decompression. With continued drift, however, a substantial reduction in lateral stiffness ("softening") results from the progression of gap opening along the base joint of the wall as well as from nonlinear behavior of concrete in compression. The point at which softening is apparent is referred to as the effective linear limit. The base shear and lateral drift corresponding to the effective linear limit are denoted as V_{ell} and Θ_{ell} respectively. V_{ell} can be related to the base shear demand from a seismic design code to control the lateral force level at softening of a UPT wall. Since softening usually develops in a smooth and continuous manner[2], the term effective linear limit is used to describe this point on the lateral load response of a wall. As a result of the smooth softening behavior, there is no specific stress condition associated with this point.

INITIATION OF COVER SPALLING

Cover spalling initiates when the ultimate unconfined concrete strain is reached at the ends of the wall base. The base shear and lateral drift corresponding to the initiation of cover spalling are denoted as V_{spl} and Θ_{spl} respectively.

YIELDING OF POST-TENSIONING STEEL

Yielding of the PT steel occurs when the PT yield strain is reached. The base shear and lateral drift corresponding to the linear limit strain of the outermost PT steel are denoted as V_{llp} and Θ_{llp} respectively. Due to unbonding, the yield strain of the PT steel is typically reached after the effective linear limit (ELL) is reached (and thus after significant softening occurs)[2,3].

BASE SHEAR CAPACITY

The base shear capacity is intended to be controlled by axial-flexural behavior rather than by shear sliding at the base. Thus, the overturning capacity of the wall controls the base shear capacity. The base shear capacity occurs between the limit states of yielding of the PT steel (LLP) and crushing of the confined concrete (CCC), and is denoted as V_{max}.

LOSS OF PRESTRESS

Prestress is lost in a UPT precast concrete wall under cyclic lateral load when the wall is unloaded from a drift which exceeds the drift at which the PT steel yields, Θ_{llp}. The prestress loss depends on the magnitude of inelastic strain in the PT steel prior to unloading.

CRUSHING OF CONFINED CONCRETE

Failure of a UPT precast concrete wall occurs when the confined concrete at the base of the wall fails in compression. This occurs when the confining reinforcement fractures and the concrete confinement is lost. Significant loss of lateral load and gravity load resistance is expected to occur when crushing of the confined concrete occurs. The base shear and lateral drift corresponding to crushing of the confined concrete are denoted as V_{ccc} and Θ_{ccc} respectively.

ANALYTICAL MODELS

Two types of analytical models are considered in this study: (1) a simple analytical model that uses mathematical formulae to estimate the critical points in a tri-linear idealization of the nonlinear lateral force-lateral drift behavior of UPT walls; and (2) a finite element model for UPT walls that uses fiber elements to model the precast concrete wall panels and nonlinear truss elements to model the unbonded post-tensioning (PT) steel. Each model is formulated to predict critical flexural limit states in the lateral force versus lateral drift behavior of UPT walls. This section presents the simple analytical model developed by Perez et al.[5,8], and summarizes the UPT wall model based on fiber elements developed by Kurama et al.[2]

SIMPLE MODEL (SM)

The simple model (SM) is based on the tri-linear idealized base shear versus lateral drift behavior shown in Fig. 2, and uses "simple" formulae to estimate the base shear and lateral drift at the points ELL, LLP, and CCC, which define the idealization. The SM applies to a generalized UPT wall comprised of *r* one-story-tall wall panels, three groups of PT steel with different initial prestress forces, and eccentric gravity loads whose magnitudes and eccentricities vary along the height of the wall. Perez et al.[5] provide a detailed development of the SM and the related formulae, and present a performance-based seismic design methodology for UPT walls that uses the SM to estimate UPT wall capacities.

Fig. 3 shows the forces acting on a generalized UPT wall, which are: (1) lateral loads transmitted to the wall by the floor and roof diaphragms ($F_{w,i}$); (2) a wall base shear force (V_w) that is in equilibrium with the lateral loads; (3) a concentrated moment at each floor level ($M_{N,i}$) produced by a gravity load (N_i) acting at an eccentricity ($e_{N,i}$), where N_i accounts for loads supported by the wall and the wall self-weight; (4) post-tensioning forces in three groups of PT steel (T_1, T_2, and T_3); and (5) a concrete compression stress resultant at the base (C). The wall length, height, and contact length at the base are denoted as l_w, H_w, and c, respectively.

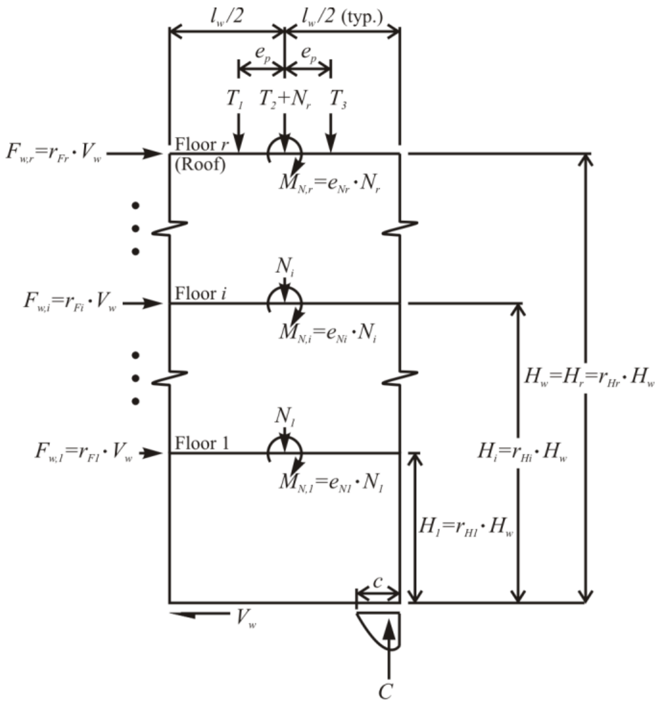

Fig. 3 Forces on a generalized UPT wall

Softening in a UPT wall occurs from gap opening along the base or from nonlinear behavior of concrete in compression. The base shear at ELL, V_{ell}, is:

$$V_{ell} = \min\left\{ \begin{array}{l} V_{ell-1} = \dfrac{T_1\left(\dfrac{l_w}{2}+e_p\right)+\left(T_2+N\right)\dfrac{l_w}{2}+T_3\left(\dfrac{l_w}{2}-e_p\right)-M_N-C\left(\dfrac{a}{2}\right)}{H_w\sum\limits_{i=1,r}\left(r_{Hi}\cdot r_{Fi}\right)} \\ V_{ell-2} = 2.5V_{dec} \end{array} \right\} \quad (1)$$

where $N=\sum\limits_{i=1,r}N_i$; $M_N=\sum\limits_{i=1,r}M_{N,i}$; $C=T_1+T_2+T_3+N$; $T_1=T_{1i}$; $T_2=T_{2i}$; $T_3=T_{3i}$; and $a=\dfrac{C}{0.85f_c'\cdot t_w}$.

T_{1i}, T_{2i}, and T_{3i} represent the initial prestress force in each PT steel group. N is the total gravity load supported by the wall at the base and M_N is the total overturning moment due to possibly eccentric gravity loads. C is the compression resultant at the base of the wall. V_{ell} is defined as the smaller of V_{ell-1} and V_{ell-2}; V_{ell-1} accounts for softening due to nonlinear behavior of concrete in compression and V_{ell-2} accounts for gap opening along the wall base. The term a is the depth of the equivalent compression stress block, f_c' is the unconfined concrete compressive strength, and t_w is the wall thickness. The term r_{Hi} represents the ratio of the height of floor level i to the wall height. The terms r_{Fi} and r_{Fr} represent the fraction of the total base shear applied at floor level i and at the roof, respectively. V_{dec} in Eq. (1) is calculated using the expression in Eq. (1) for V_{ell-1}, except that the term (a/2) is replaced by (l_w/3).

The roof lateral drift at ELL, Θ_{ell}, from an elastic analysis of a cantilevered wall is:

$$\Theta_{ell} = \frac{(\Delta_{Fr,ell} + \Delta_{Sr,ell} + \Delta_{Nr,ell} + \Delta_{Pr,ell})}{H_w} \tag{2}$$

where $\Delta_{Fr,ell} = \sum_{i=1,r} \frac{1}{2E_c \cdot I_w} (r_{Fi} \cdot V_{ell}) \cdot r_{Hi}^{\ 2} \cdot H_w^{\ 3} \left(r_{Hr} - \frac{1}{3} r_{Hi} \right)$;

$\Delta_{Sr,ell} = \sum_{i=1,r} \frac{1}{G_c \cdot A_w'} (r_{Fi} \cdot V_{ell} \cdot r_{Hi} \cdot H_w)$;

$\Delta_{Nr,ell} = \sum_{i=1,r} \frac{1}{E_c \cdot I_w} \cdot M_{N,i} (r_{Hi} \cdot H_w) \cdot H_w \left(r_{Hr} - \frac{1}{2} r_{Hi} \right)$;

$\Delta_{Pr,ell} = \frac{e_p (T_3 - T_1) \cdot H_w^{\ 2}}{2E_c \cdot I_w}$; $T_1 = T_{1i}$; and $T_3 = T_{3i}$.

The terms $\Delta_{Fr,ell}$, $\Delta_{Nr,ell}$, and $\Delta_{Pr,ell}$ represent the elastic roof deflections of the wall in flexure at ELL due to lateral loads, eccentric gravity loads, and differential prestress forces, respectively. $\Delta_{Sr,ell}$ is the roof deflection due to elastic shear deformations. G_c is the shear modulus of concrete, A_w' is the effective shear area of the wall, E_c is the elastic modulus of concrete, and I_w is the uncracked moment of inertia of the wall. V_{ell} is computed using Eq. (1).

The derivation of V_{llp} is based on the following assumptions: (1) plane sections remain plane in the concrete only (due to unbonding, strain compatibility between the PT steel and the surrounding concrete does not exist); (2) the cover concrete is spalled and is excluded; (3) the wall is underreinforced; (4) equivalent stress block parameters for confined concrete, α and β, correspond to the ultimate strain of the confined concrete, ε_{ccc} (i.e., α = 0.9 and β = 1.0 as given by Paulay and Priestley[9]); and (5) the wall pivots about the neutral axis (NA) location. An iterative procedure[5] to calculate V_{llp} is summarized as follows:

1. Calculate the equivalent confined concrete stress block length, a'' as:

$$a'' = \frac{T_1 + T_2 + T_3 + N}{\alpha \cdot f_{cc}' \cdot t_w''} \tag{3}$$

where $\alpha = 0.9$; $T_1 = f_{py} \cdot A_{p1}$; $T_2 = f_{py} \cdot A_{p2}$; and $T_3 = f_{py} \cdot A_{p3}$. The term f_{cc}' represents the confined concrete compression strength, which can be obtained from experiments or from an empirical confined concrete stress-strain model[10,11]. The terms a'' and t_w'' are similar to a and t_w, except that they exclude the concrete cover and are measured from the centerline of the confining reinforcement. A_{p1}, A_{p2}, and A_{p3} represent the PT steel area in PT steel groups 1, 2, and 3, respectively. f_{py} represents the yield stress of the PT steel. The three PT steel groups are assumed to be yielded in the first iteration, and the forces in PT steel groups 2 and 3 are then adjusted by the iteration process.

2. Identify the location of the NA by calculating the post-spalling contact length at the base, c'', which excludes the thickness of the spalled cover:

$$c'' = \frac{a''}{\beta} \tag{4}$$

3. Define the location of each PT steel group from the NA location:

$$l_1 = \frac{l''_w}{2} - c'' + e_p \text{ ; } l_2 = \frac{l''_w}{2} - c'' \text{; and } l_3 = \frac{l''_w}{2} - c'' - e_p \tag{5}$$

4. Calculate the gap opening width at the location of PT steel group 1, Δ_{v1} when the gap at the base of the wall has caused the PT steel in group 1 to yield:

$$\Delta_{v1} = \frac{\left(f_{py} - f_{p1i}\right)}{E_p} \cdot H_{unb} \tag{6}$$

where f_{p1i} represents the initial stress in the PT steel in group 1. E_p is the modulus of elasticity of the PT steel, and H_{unb} is the unbonded height of the PT steel.

5. Calculate the strain in the PT steel in each group (ε_{p1}, ε_{p2}, and ε_{p3}) when the gap at the base of the wall has caused the PT steel in group 1 to yield:

$$\varepsilon_{p1} = \frac{f_{py}}{E_p} \text{ ; } \varepsilon_{p2} = \frac{f_{p2i}}{E_p} + \frac{\Delta_{v1}}{H_{unb}} \cdot \left(\frac{l_2}{l_1}\right) \text{; and } \varepsilon_{p3} = \frac{f_{p3i}}{E_p} + \frac{\Delta_{v1}}{H_{unb}} \cdot \left(\frac{l_3}{l_1}\right) \tag{7}$$

where f_{p2i} and f_{p3i} represent the initial stresses in the PT steel in groups 2 and 3, respectively. l_1, l_2, and l_3 are from Eq. (5). In Eq. (7), the strain for PT steel groups 2 and 3, ε_{p2} and ε_{p3}, respectively, are the sum of the initial strain in the PT steel due to prestressing plus the change in strain in the PT steel due to gap opening at the base of the wall.

6. Calculate the force in each group of PT steel (T_1, T_2, and T_3):

$$T_1 = (\varepsilon_{p1} \cdot E_p \cdot A_{p1}) \text{; } T_2 = (\varepsilon_{p2} \cdot E_p \cdot A_{p2}) \text{; and } T_3 = (\varepsilon_{p3} \cdot E_p \cdot A_{p3}) \tag{8}$$

where ε_{p1}, ε_{p2}, and ε_{p3} are from Eq. (7).

7. From vertical equilibrium at the base of the wall, calculate a new NA location, c''_{new}:

$$c''_{new} = \frac{T_1 + T_2 + T_3 + N}{\alpha \cdot f'_{cc} \cdot \beta \cdot t''_w} \tag{9}$$

where T_1, T_2, and T_3 are calculated from Eq. (8).

Steps 3 through 7 are repeated iteratively until c''_{new} converges; convergence is usually achieved within three iterations. The value of c''_{new} at the end of the iteration procedure is defined as c''_{llp}.

The base shear at yielding of the PT steel, V_{llp} is:

$$V_{llp} = \frac{T_1\left(l_1 + \frac{\beta \cdot c''_{llp}}{2}\right) + \left(T_2 + N\right)\left(l_2 + \frac{\beta \cdot c''_{llp}}{2}\right) + T_3\left(l_3 + \frac{\beta \cdot c''_{llp}}{2}\right) - M_N}{H_w \sum_{i=1,r}\left(r_{Hi} \cdot r_{Fi}\right)} \tag{10}$$

where c''_{llp}, l_1, l_2, l_3, T_1, T_2, and T_3 are obtained from the iteration.

The roof lateral drift at LLP, Θ_{llp} is estimated as:

$$\Theta_{llp} = \frac{(\Delta_{go,llp} + \Delta_{Fr,llp} + \Delta_{Sr,llp} + \Delta_{Nr,llp} + \Delta_{Pr,llp})}{H_w} \tag{11}$$

where $\Delta_{go,llp} = \frac{\Delta_{v1} \cdot H_w}{l_1}$; $\Delta_{Fr,llp} = \sum_{i=1,r} \frac{1}{2E_c \cdot I_w}\left(r_{Fi} \cdot V_{llp}\right) \cdot r_{Hi}{}^2 \cdot H_w{}^3\left(r_{Hr} - \frac{1}{3} r_{Hi}\right)$;

$\Delta_{Sr,llp} = \sum_{i=1,r} \frac{1}{G_c \cdot A'_w}\left(r_{Fi} \cdot V_{llp} \cdot r_{Hi} \cdot H_w\right)$;

$\Delta_{Nr,llp} = \sum_{i=1,r} \frac{1}{E_c \cdot I_w} \cdot M_{N,i}(r_{Hi} \cdot H_w) \cdot H_w\left(r_{Hr} - \frac{1}{2} r_{Hi}\right)$;

$\Delta_{Pr,llp} = \frac{e_p\left(T_3 - T_1\right) \cdot H_w{}^2}{2E_c \cdot I_w}$; and T_1, and T_3 are from Eq. (8). $\Delta_{go,llp}$ is the roof deflection of the wall due to rigid-body rotation from gap opening at the base. The terms $\Delta_{Fr,llp}$, $\Delta_{Nr,llp}$, and $\Delta_{Pr,llp}$ represent the elastic roof deflections of the wall in flexure at LLP due to lateral loads, eccentric gravity loads, and different forces in the PT steel, respectively. $\Delta_{Sr,llp}$ is the roof deflection of the wall at LLP due to elastic shear deformations.

Neglecting strain hardening in the PT steel, the base shear is essentially constant[5] between LLP and CCC, thus, V_{ccc} equals V_{llp}. The roof lateral drift at CCC, Θ_{ccc} is estimated as:

$$\Theta_{ccc} = \frac{(\Delta_{rbr,ccc} + \Delta_{Fr,ccc} + \Delta_{Sr,ccc} + \Delta_{Nr,ccc} + \Delta_{Pr,ccc})}{H_w} \tag{12}$$

where $\Delta_{rbr,ccc} = \left(\frac{\varepsilon_{ccc}}{c''_{ccc}} \cdot H_{cr} \cdot H_w\right)$; $c''_{ccc} = c''_{llp}$; $H_{cr} = \min(\lambda_{ccc1} \cdot t''_w, \lambda_{ccc2} \cdot c''_{ccc})$;

$\varepsilon_{ccc} = \psi \cdot \varepsilon_{cu}$;

$\Delta_{Fr,ccc} = \sum_{i=1,r} \frac{1}{2E_c \cdot I_w}\left(r_{Fi} \cdot V_{ccc}\right) \cdot \left(r_{Hi} \cdot H_w - H_{cr}\right)^2 \cdot \left[H_w - H_{cr} - \frac{1}{3} \cdot \left(r_{Hi} \cdot H_w - H_{cr}\right)\right]$;

$\Delta_{Sr,ccc} = \sum_{i=1,r} \frac{1}{G_c \cdot A'_w}\left[r_{Fi} \cdot V_{ccc} \cdot \left(r_{Hi} \cdot H_w - H_{cr}\right)\right]$;

$\Delta_{Nr,ccc} = \sum_{i=1,r} \frac{1}{E_c \cdot I_w} \cdot M_{N,i}\left(r_{Hi} \cdot H_w - H_{cr}\right) \cdot \left[H_w - H_{cr} - \frac{1}{2}\left(r_{Hi} \cdot H_w - H_{cr}\right)\right]$;

$\Delta_{Pr,ccc} = \frac{e_p\left(T_3 - T_1\right) \cdot \left(H_w - H_{cr}\right)^2}{2E_c \cdot I_w}$; $M_{N,i} = e_{Ni} \cdot N_i$; $M_{N,r} = e_{Nr} \cdot N_r$; and T_1 and T_3 are from Eq. (8). $\Delta_{rbr,ccc}$ is the roof deflection of the wall at CCC due to rigid-body rotation at the base assuming a constant curvature over the height of the confined concrete failure zone near the wall base, H_{cr}. The parameters λ_{ccc1} and λ_{ccc2} are used to estimate H_{cr} and in the present paper, both parameters are set equal to 2. The terms $\Delta_{Fr,ccc}$, $\Delta_{Nr,ccc}$, and $\Delta_{Pr,ccc}$ represent the elastic roof deflections of the wall in flexure at CCC (neglecting elastic deflections within H_{cr}) due to lateral loads, eccentric gravity loads, and different forces in the PT steel, respectively. $\Delta_{Sr,ccc}$ is the roof deflection of the wall at CCC due to elastic shear deformations above H_{cr}. The confined concrete crushing strain, ε_{ccc} at the extreme compression edge of the wall is $\psi\,\varepsilon_{cu}$, where ε_{cu} is the estimated ultimate strain capacity of the confined concrete from experimental data or an empirical confined concrete stress-strain model[10,11]. The parameter ψ reduces ε_{cu} to account for the confined concrete crushing behavior observed in the experimental study described later. In this study, values of ψ equal to 0.95 and 0.75 were used in analyses of the test walls described later to compare with experimental results under monotonic loading and cyclic loading, respectively. Results for ψ equal to 1.0 are also used to compare with experimental data.

FIBER MODEL (FM)

The finite element model for UPT walls developed by Kurama et al.[2], referred to as the "fiber model" (FM), uses fiber beam-column elements to model the precast concrete wall panels and nonlinear truss elements to model the PT steel. Fig. 4 shows a FM for the UPT test wall described later. The DRAIN-2DX program[12] was used to develop the FM. The wall panels include well-confined concrete (near the extreme fibers of the bottom two panels) and unconfined concrete (within the bottom panels and throughout the remaining panels). Fibers with different uniaxial stress-strain curves are used to model the well-confined concrete and unconfined concrete. The typical arrangement of fibers is explained by Kurama et al.[2] A critical parameter in the fiber model is the height of the first element segment at the base of the model, which controls the lateral drift[2] at CCC, Θ_{ccc}. In the present study, the height of the first element segment at the base of the model equals H_{cr}, defined earlier. As shown in Fig. 4, the truss bars that model the PT steel are constrained to the wall panels only at the location of the PT steel anchorage at the top of the wall. All FM analyses are carried out until the confined concrete crushing strain, ε_{ccc} reaches a value of ε_{cu} (i.e., ψ = 1.0). Results are also reported for values of ψ equal to 0.95 and 0.75 to compare with experimental results under monotonic and cyclic loading, respectively.

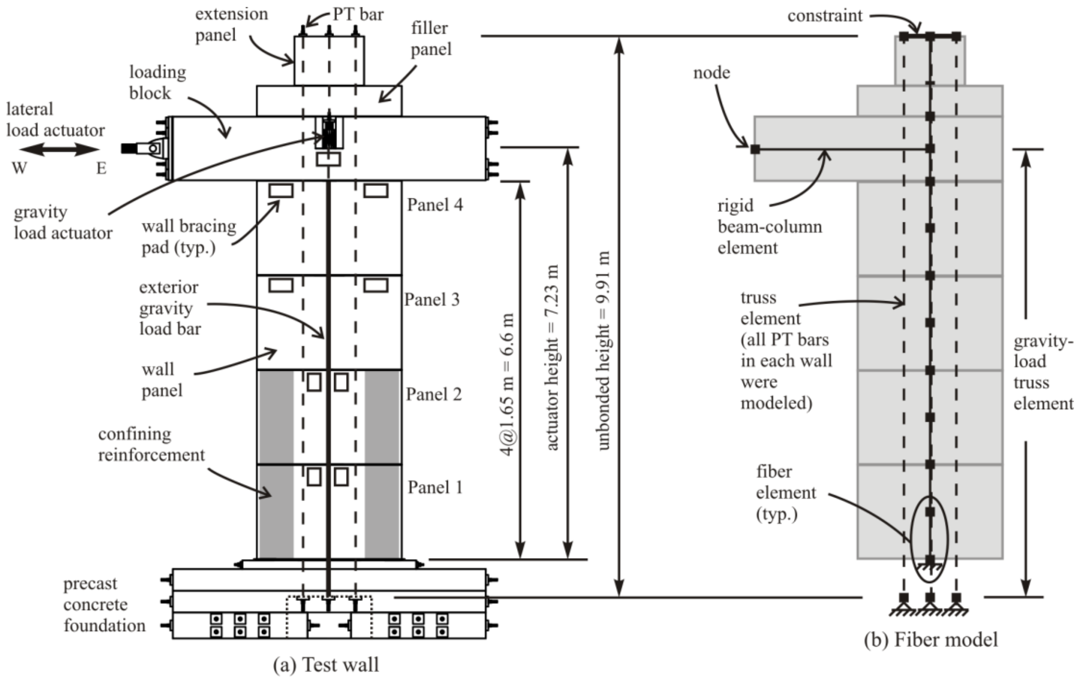

Fig. 4 Test wall configuration and associated fiber model

SUMMARY OF EXPERIMENTAL PROGRAM

TEST WALL

Fig. 4(a) shows schematically a typical test wall, which simulates the reduced-scale UPT wall from Fig. 1. Each test wall is comprised of four wall panels (numbered sequentially from the base), a loading block, a filler panel, and an extension panel, which are grouted along horizontal joints. The test wall is attached to a precast concrete foundation using unbonded PT steel that is anchored at the top of the extension panel and within the foundation. The PT steel consists of 31.8-mm (1.25-in.) diameter threadbars.

The four wall panels of the test wall represent the bottom four panels of the reduced-scaled wall (see Figs. 1(b) and 4(a)). Confining reinforcement, as shown by the shaded regions in Fig. 1, is provided in test wall Panel 1. To preserve the second story panel’s integrity and thus enable reuse throughout the experimental program, similar confining reinforcement is provided in test wall Panel 2.

The loading block, which rests on Panel 4, is used to apply gravity and lateral loads to each test wall. The gravity load is applied through an external high strength steel bar on each side of the wall using a hydraulic jack. The gravity load jacks are mounted on the loading block and exert a compressive force along the test wall centerline. The gravity load bars are anchored within the foundation using a rocker that allows the bars to pivot at the base. During each test, the applied gravity load was essentially constant at 532 kN (119.5 kips). This applied gravity load, together with the test wall self-weight of 240 kN (53.9 kips), generates a total vertical load at the base of the test wall of 772 kN (173.4 kips), which is the same as the total vertical load supported by the reduced-scale wall at the base.

As shown in Fig. 4, the lateral load actuator is attached to the west end of the loading block and exerts a lateral load in the east-west direction at a height, H_{act} of 7.23 m (23.73 ft) from the base of the wall. The single lateral load represents the resultant of a triangular inertia force profile (Fig. 1(b)). The moment-to-shear ratio at the base of the test wall is the same as that produced by a triangular inertia force profile on the reduced-scale wall.

As shown in Fig. 4, a filler panel and an extension panel are attached to the top of the loading block. Owing to lab constraints, the height of the test wall, from the base of Panel 1 to the top of the extension panel, was less than the height of the reduced-scale wall. However, the reduced-scale wall and the test wall have the same PT steel unbonded height, H_{unb} (9.91 m [32.5 ft]), so that the strains that develop in the PT steel (shown dashed in Fig. 1(b)) are the same. This unbonded height is achieved for the test wall by providing the filler and extension panels and by anchoring the PT steel deep within the foundation.

All horizontal joints between test wall panels were grouted using non-shrink grout with specified compressive strength greater than the test wall panel unconfined concrete strength. The grouted joints were typically 13 mm (0.5 in.) thick, except for the grout pad at the base joint which was 25 mm (1 in.) thick. To reduce the deterioration in the bottom two joints, 19-mm (0.75-in.) -long nylon fibers were mixed into the grout at a dosage of 17.4 N/m^3 (3 lb/yd^3).

TEST FIXTURE

A steel test fixture was designed to restrain each test wall against out-of-plane movement. Bracing pads consisting of steel plates with Teflon are grouted onto the test wall on each face (see Fig. 4(a)). The bracing pads, which move with the test wall, slide against the machined and oiled flanges of guide beams that are attached to a steel test fixture (not shown in Fig. 4(a)). The Teflon on the machined and oiled steel surface greatly reduces the friction between the test wall and the test fixture. 1.6 mm (1/16 in.) gaps are left between the Teflon and the machined flange surfaces.

TEST MATRIX

The experimental investigation studied the effect of four parameters on the lateral load response of UPT precast concrete walls. Table 1 shows these parameters are: (1) total area of the PT steel across the horizontal joints, A_p; (2) initial stress in the PT steel, f_{pi} (normalized with respect to the ultimate strength of the PT steel, f_{pu}); (3) initial stress in the concrete due to post-tensioning, $f_{ci,p}$; and (4) confining reinforcement details in the base panel. These parameters were selected to produce a significant variation in the lateral load response.

Table 1 Test matrix

Test Wall	Loading	A_p (cm^2)	f_{pi}/f_{pu}	$f_{ci,p}$ (MPa)	Confinement Type	PT bar arrangement[a]
TW1	Monotonic	48.4	0.553	8.20	Spirals	xx xox xx
TW2	Cyclic	48.4	0.553	8.20	Spirals	xx xox xx
TW3	Cyclic	48.4	0.553	8.20	Hoops	xx xox xx
TW4	Cyclic	48.4	0.277	4.07	Hoops	xx xox xx
TW5	Cyclic	24.2	0.553	4.07	Hoops	xo oxo ox

1 cm^2 = 0.155 in.2; 1MPa = 0.145 ksi.

[a] x = bar and o = no bar in locations shown in Fig. 1(d). PT bars are numbered for each test wall sequentially from left to right using the notation PT1, PT2, etc.

For brevity, the test walls are named TW1 through TW5. TW1 was tested under gravity and monotonic lateral loading, while TW2 through TW5 were tested under gravity and cyclic lateral loading with a loading history typically consisting of the following lateral drift cycles: three cycles each at 0.05%, 0.1%, 0.25%, 0.5%, 0.1%, 1%, 1.5%, 2%, 0.1%, 3% where applicable, and additional cycles beyond 3% as necessary to reach failure. The target drifts were selected to displace the walls to drift levels between the limit states identified earlier. On average, the total gravity load was 3.7% of $f'_c\, A_g$, where A_g represents the gross cross-sectional area of the test walls.

The bottom two panels of TW1 and TW2 have spiral confining reinforcement as shown in Fig. 1(d), while the bottom two panels of TW3 through TW5 have hoop confining reinforcement, also shown in Fig. 1(d). The upper two panels for all test walls are lightly reinforced using two curtains of 6x6-W4.0xW4.0 welded wire mesh. Fig. 1 identifies the confinement ratios for the two different confinement types, given as a volumetric ratio for spiral confined walls, ρ_{sp} and as area ratios for the hoop confined walls, $\rho_{h,lw}$ and $\rho_{h,tw}$. Table 1 shows the placement of the PT steel in each test wall.

MATERIAL PROPERTIES

Table 2 summarizes key material properties for the confined and unconfined concrete, the PT steel, and the confining reinforcement used in each test wall. The unconfined concrete strengths were obtained from cylinder tests conducted at approximately the time of each wall test. The material properties for the PT steel were obtained by testing individual PT bars with their associated anchorages[13]. The confining reinforcement (i.e., spiral wire and rebar) was tested in uniaxial tension to obtain the properties summarized in Table 2. The properties for confined concrete were derived using analytical confinement models[10,11] with input properties based on material tests. Specifically, the confinement model proposed by Mander et al.[10] was used to develop the uniaxial stress-strain curve for the hoop confined regions of TW3 through TW5, while the confinement model proposed by Oh[11] was used to develop the uniaxial stress-strain curve for the spiral confined regions of TW1 and TW2. In both models, the estimated ultimate strain capacity of the confined concrete, ε_{cu}, is based on fracture of the confining steel.[10]

Table 2 Material properties based on component tests

Test Wall	Concrete			PT steel		Confining reinforcement		
	Unconfined	Confined						
	f'_c (MPa)	f'_{cc} (MPa)	ε_{cu} (mm/mm)	f_{py} (MPa)	f_{pu} (MPa)	f_{sy} (MPa)	f_{su} (MPa)	ε_{sf} (mm/mm)
TW1	52.4	110	0.080	952	1103	414	614	0.077
TW2	52.4	110	0.080	952	1103	414	614	0.077
TW3	55.2	89.6	0.073	952	1103	432	665	0.139
TW4	55.2	89.6	0.073	952	1103	432	665	0.139
TW5	55.2	89.6	0.073	952	1103	432	665	0.139

1 MPa = 0.145 ksi.

As noted earlier, the confined concrete crushing strain, ε_{ccc} at the extreme compression edge of the wall is $\psi\,\varepsilon_{cu}$. The parameter ψ reduces ε_{cu} to account for the confined concrete crushing behavior observed in the experimental study. Values of ψ equal to 0.95 and 1.0 are used in the SM and FM analyses of TW1 (under monotonic loading), while values of ψ equal to 0.75 and 1.0 are used in the SM and FM analyses of TW2 through TW5 (under cyclic loading).

COMPARISON OF ANALYTICAL AND EXPERIMENTAL RESULTS

This section presents selected experimental results. A comprehensive report on the experimental results is provided by Perez et al.[5]

COMPARISON OF BASE-SHEAR-LATERAL-DRIFT RESPONSE UNDER MONOTONIC LOADING

Fig. 5 compares the monotonic experimental base shear versus lateral drift results with analytical results from the simple model (SM) and monotonic loading analysis results from the fiber model (FM) for TW1. The lateral drift is taken as the ratio of the lateral displacement of the loading block to the actuator height (see Fig. 4) and is expressed as a percent. The experimental curve in Fig. 5 has repeated reductions in base shear, which occurred when the test was paused and the gravity load jack in the test fixture was adjusted.

Fig. 5 shows: (1) the decompression limit state (DEC) is estimated closely by both models; (2) the effective linear limit (ELL) is estimated closely by the SM (ELL is not considered by the FM); (3) concrete spalling at the wall base (SPL) is estimated closely by the FM (SPL is not considered by the SM); (4) yielding of the PT steel (LLP) is estimated reasonably well by both models; and (5) the lateral drift at crushing of confined concrete (CCC), based on $\psi = 0.95$ (i.e., $\varepsilon_{ccc} = 0.95\text{x}0.08 = 0.076$ mm/mm), is estimated well by the SM and somewhat overestimated by the FM.

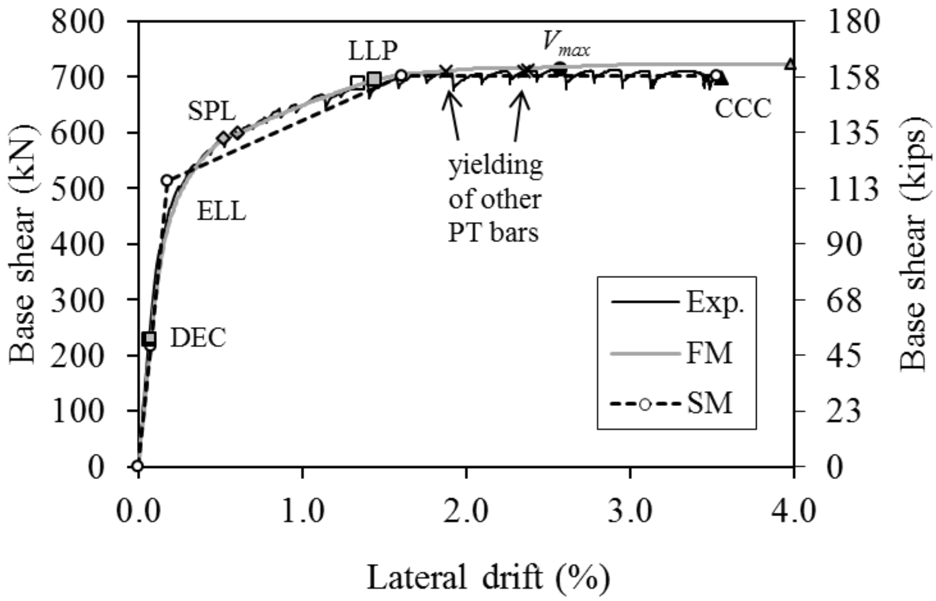

Fig. 5 Comparison of experimental and analytical results under monotonic loading (TW1)

Table 3 shows analytical and experimental base shear and lateral drift values for TW1 at specific limit states. At DEC, SPL, LLP, and CCC, the base shear values from both analytical models are within 5% of the experimental results. The analytical lateral drift results have more substantial differences from the experimental results. For Θ_{llp}, the FM results exceed the experimental results by 7% and the SM results exceed the experimental results by 18%. The FM results for Θ_{ccc} exceed the experimental results by 12% for ψ = 0.95 and 15% for ψ = 1.0. The SM results for Θ_{ccc} are within 4% of the experimental results, with a 1% difference for ψ = 0.95.

Table 3 Comparison of experimental and analytical results for TW1

Result Type	DEC		SPL		LLP		CCC	
	V_{dec} (kN)	Θ_{dec} (%)	V_{spl} (kN)	Θ_{spl} (%)	V_{llp} (kN)	Θ_{llp} (%)	V_{ccc} (kN)	Θ_{ccc} (%)
Exp.	228	0.07	598	0.61	687	1.35	699	3.56
FM, ψ = 0.95[a]	231	0.08	590	0.52	695	1.44	723	3.98 (4.11)[a]
SM, ψ = 0.95[a]	218	0.07	-	-	702	1.60	702	3.53 (3.70)[a]

1 kN = 0.2248 kips.

[a]results are for ψ = 0.95, except for results in parentheses which are for ψ = 1.0.

COMPARISON OF BASE-SHEAR-LATERAL-DRIFT RESPONSE UNDER CYCLIC LOADING

Fig. 6 compares the cyclic experimental base shear versus lateral drift results with cyclic and monotonic loading analysis results from the fiber model (FM) for TW2. Fig. 6 shows: (1) the FM cyclic lateral load response closely approximates the experimental cyclic response of TW2; (2) the FM monotonic response produces a good upper bound to the experimental cyclic response; and (3) the FM monotonic response with ψ = 0.75 results in a better estimation of the lateral drift at CCC than with ψ = 1.0.

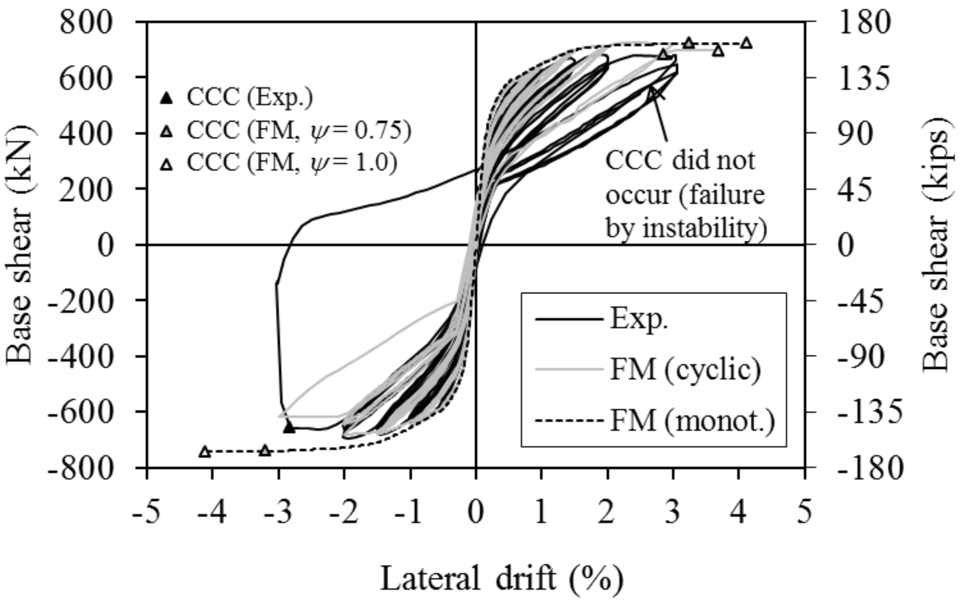

Fig. 6 Comparison of experimental and analytical results under cyclic loading (TW2)

Table 4 shows analytical and experimental base shear and lateral drift values for TW2 at specific limit states. Fig. 7 compares the experimental envelope lateral load response of TW2 to monotonic analysis results using the FM and SM. The experimental envelope response was obtained by plotting the maximum base shear response under cyclic loading. Table 4 includes analytical results for ψ = 0.75 and ψ = 1.0; however, Fig. 7 only shows analytical results based on ψ = 0.75 (only CCC is affected by ψ).

Table 4 Comparison of experimental and analytical results for TW2

Result Type	DEC		SPL		LLP		CCC	
	V_{dec} (kN)	Θ_{dec} (%)	V_{spl} (kN)	Θ_{spl} (%)	V_{llp} (kN)	Θ_{llp} (%)	V_{ccc} (kN)	Θ_{ccc} (%)
Exp. (east)	200	0.07	594	0.65	671	1.44	682[a]	3.04[a]
Exp. (west)	207	0.08	579	0.57	673	1.51	658	2.83
FM[c], $\psi = 0.75$[b]	243	0.09	592	0.52	707	1.46	685 (696)[b]	2.86 (3.69)[b]
FM[m], $\psi = 0.75$[b]	231	0.08	590	0.52	695	1.44	723	3.23 (4.11)[b]
SM, $\psi = 0.75$[b]	218	0.07	-	-	702	1.60	702	2.83 (3.70)[b]

1 kN = 0.2248 kips.
[a]CCC limit state was not reached due to instability failure of base panel and values of V and Θ correspond to the maximum Θ value reached in previous cycles.
[b]results are for $\psi = 0.95$, except for results in parentheses which are for $\psi = 1.0$.
[c]cyclic loading.
[m]monotonic loading.

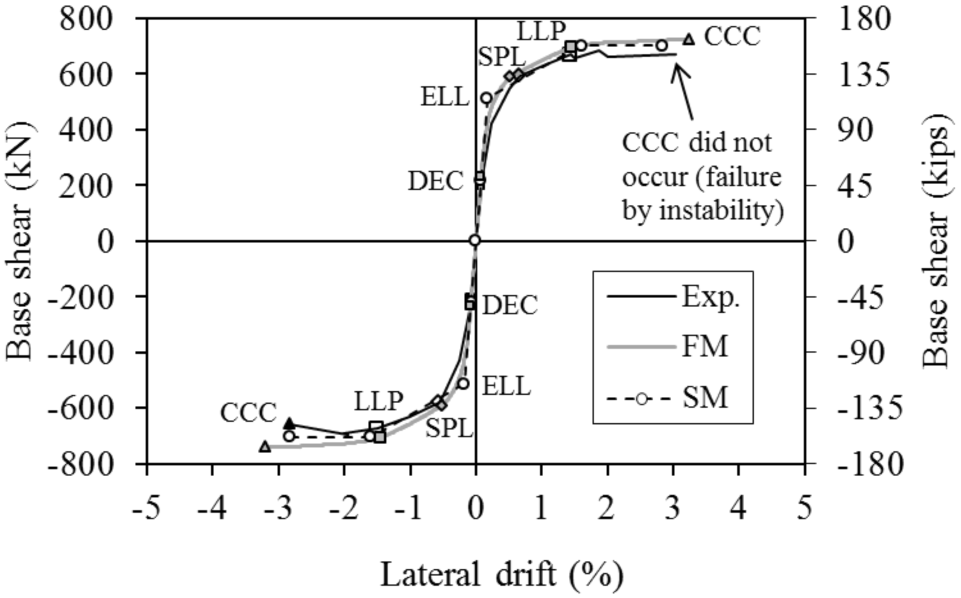

Fig. 7 Comparison of experimental envelope and analytical monotonic results (TW2)

Fig. 7 and Table 4 show that at SPL, LLP, and CCC, the base shear values from both analytical models are within 5% of the experimental results (where appropriate, average experimental values under eastward- and westward loading are used as the basis for comparison). The FM result for V_{dec} is overestimated by as much as 19% for cyclic analysis and by 14% for monotonic analysis. The SM overestimates V_{dec} by 7%.

The analytical lateral drift results are within 15% of the experimental results, with Θ_{ccc} being as close as 1% from the experimental value. In general, the base shear and lateral drift response values from monotonic FM analysis (shown in Fig. 7) are in better agreement with the experimental results than are the results form cyclic FM analysis. The base shear and lateral drift results from the SM are within 9% of the experimental results.

Referring to Fig. 6, TW2 failed by crushing of the confined concrete (CCC) during the first westward half-cycle to a 3% drift. After CCC occurred at the west end, additional half-cycles to the east were introduced at a drift of 3%, resulting in a buckling failure in the confined concrete region of the base panel. This undesirable failure mode was mitigated by modifying the confining reinforcement, which included the replacement of spirals with hoops as shown in Fig. 1(d).

Fig. 8 compares the cyclic experimental base shear versus lateral drift results with cyclic and monotonic loading analysis results from the fiber model (FM) for TW3. Fig. 8 shows: (1) the FM cyclic lateral load response closely approximates the experimental cyclic response of TW3 for eastward loading; (2) the FM monotonic response produces a good upper bound to the experimental cyclic response; (3) the FM cyclic response with ψ = 1.0 results in a slightly better estimation of the lateral drift at CCC than with ψ = 0.75; and (4) the FM monotonic response with ψ = 0.75 results in a better estimation of the lateral drift at CCC than with ψ = 1.0.

As shown in Fig. 8, The experimental response under westward loading (i.e., negative lateral drift values) is weaker than that for eastward loading due to poor consolidation of the concrete in the confined concrete region at the west end of the base panel.[5] Therefore, the accuracy of analytical models is established using experimental results under eastward loading, corresponding to positive lateral drift values.

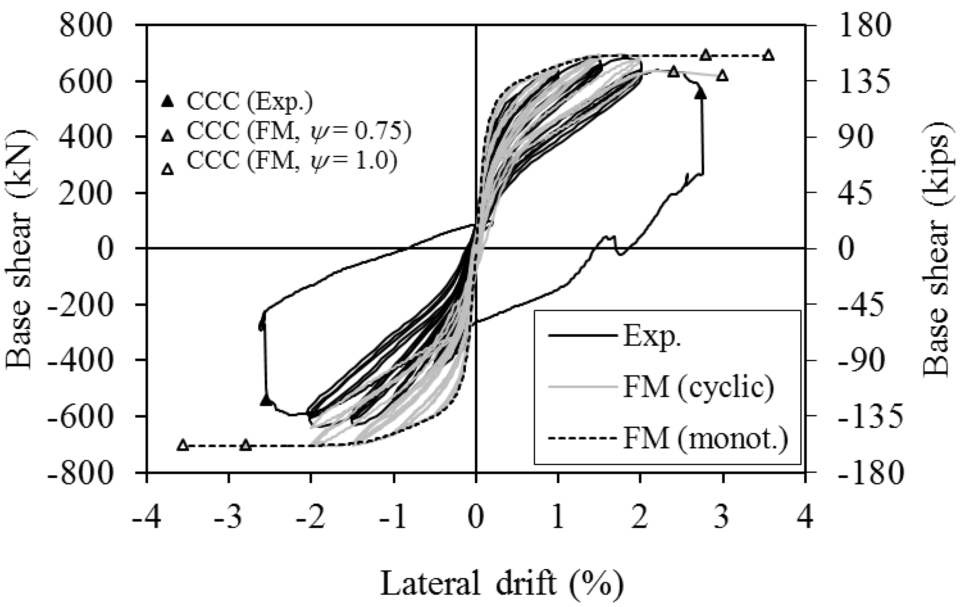

Fig. 8 Comparison of experimental and analytical results under cyclic loading (TW3)

Table 5 shows analytical and experimental base shear and lateral drift values for TW3 at specific limit states. Fig. 9 compares the experimental envelope lateral load response of TW3 to monotonic analysis results using the FM and SM. Table 5 includes analytical results for ψ = 0.75 and ψ = 1.0; however, Fig. 9 only shows analytical results based on ψ = 0.75 (only CCC is affected by ψ). Table 5 includes experimental and analytical results for both eastward and westward loading, but (as mentioned above) only eastward experimental values are used to verify the FM and SM results.

Table 5 Comparison of experimental and analytical results for TW3

Result Type	DEC		SPL		LLP		CCC	
	V_{dec} (kN)	Θ_{dec} (%)	V_{spl} (kN)	Θ_{spl} (%)	V_{llp} (kN)	Θ_{llp} (%)	V_{ccc} (kN)	Θ_{ccc} (%)
Exp. (east)	246	0.07	620	0.83	670	1.63	556	2.74
Exp. (west)	242	0.07	330	0.13	604	1.54	542	2.54
FM[c], ψ = 0.75[b]	219	0.06	567	0.40	714	1.47	631 (617)[b]	2.40 (3.00)[b]
FM[m], ψ = 0.75[b]	223	0.06	589	0.46	691	1.44	699 (697)[b]	2.80 (3.55)[b]
SM, ψ = 0.75[b]	218	0.06	-	-	693	1.58	693	2.85 (3.75)[b]

1 kN = 0.2248 kips.
[b]results are for ψ = 0.95, except for results in parentheses which are for ψ = 1.0.
[c]cyclic loading.
[m]monotonic loading.

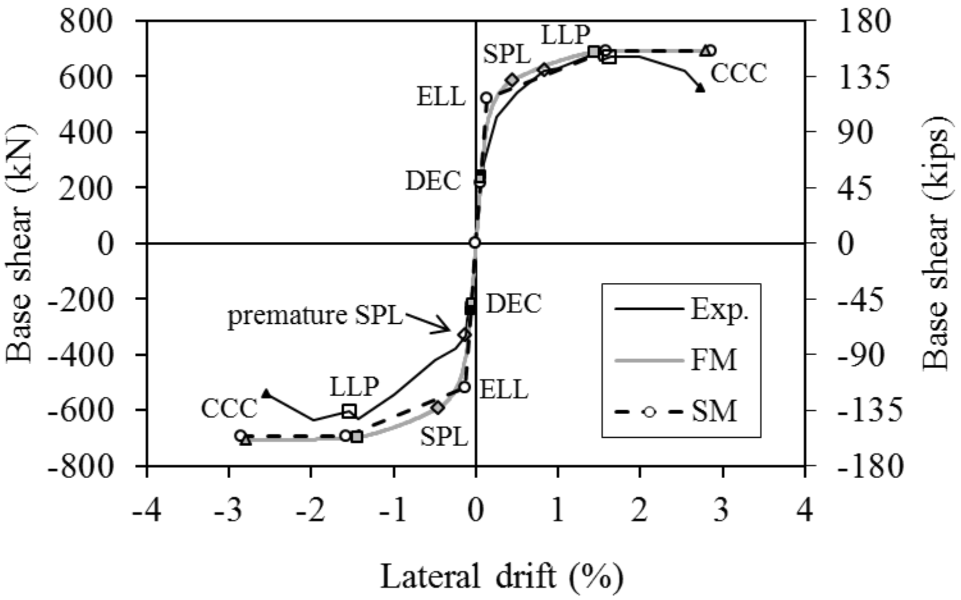

Fig. 9 Comparison of experimental envelope and analytical monotonic results (TW3)

Fig. 9 and Table 5 show that at DEC, SPL, LLP, and CCC, the base shear values from both analytical models are within 14% of the experimental results. V_{ccc} is overestimated by as much as 26% using monotonic FM analysis. However, based on cyclic FM analysis with ψ = 1.0, V_{ccc} is overestimated by 11% (see Fig. 8). The SM overestimates V_{ccc} by about 25% because it does not account for strength loss due to cyclic loading.

The lateral drift result at SPL, Θ_{spl}, is underestimated by the FM by about 50% (SPL is not considered by the SM.) Θ_{dec} and Θ_{llp} are underestimated by the FM by 14% and 12%, respectively. The SM underestimates Θ_{dec} and Θ_{llp} by 14% and 3% respectively. The cyclic FM with ψ = 1.0 overestimates V_{ccc} and Θ_{ccc} by 11% and 10%, respectively, while the monotonic FM with ψ = 0.75 overestimates Θ_{ccc} by only 2%. The SM with ψ = 0.75 overestimates Θ_{ccc} by 4%.

Fig. 10 compares the cyclic experimental base shear versus lateral drift results with cyclic and monotonic loading analysis results from the fiber model (FM) for TW4. Fig. 10 shows: (1) the FM cyclic lateral load response consistently overestimates the experimental cyclic base shear response of TW4; (2) the FM monotonic response produces a good upper bound to the experimental cyclic response; (3) the FM cyclic response with ψ = 1.0 results in a better estimation of the lateral drift at CCC than with ψ = 0.75; and (4) the FM monotonic response with ψ = 0.75 results in a better estimation of the lateral drift at CCC than with ψ = 1.0.

Fig. 10 shows that the cyclic FM base shear response exceeds the monotonic FM response. This occurs due to equilibrium errors in the FM resulting from overshoot tolerances that were relaxed so that the analysis could be completed[5]. This equilibrium error was observed for both TW4 and TW5, which are lightly-prestressed walls (see Table 1.)

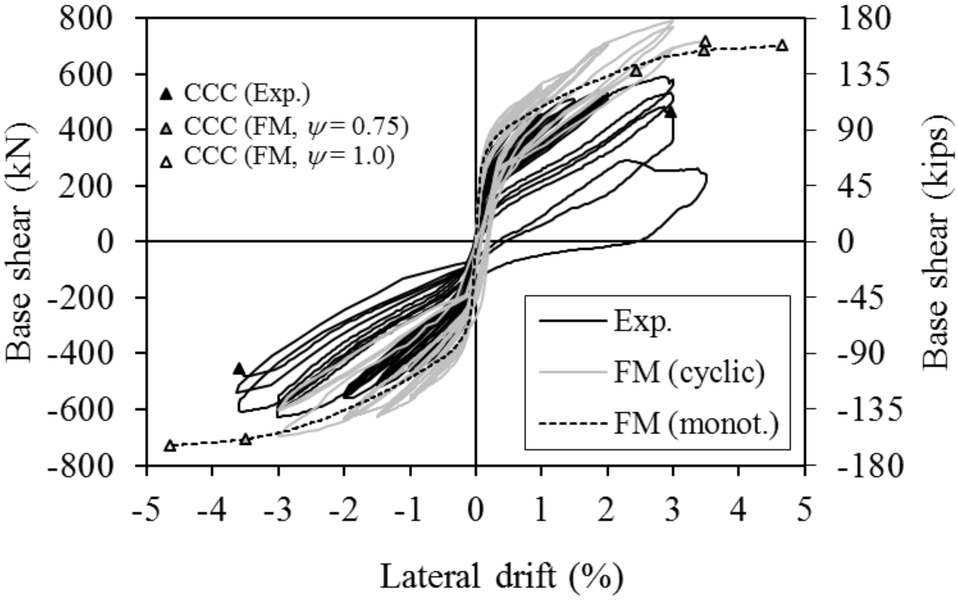

Fig. 10 Comparison of experimental and analytical results under cyclic loading (TW4)

Table 6 shows analytical and experimental base shear and lateral drift values for TW4 at specific limit states. Fig. 11 compares the experimental envelope lateral load response of TW4 to monotonic analysis results using the FM and SM. Table 6 includes analytical results for $\psi = 0.75$ and $\psi = 1.0$; however, Fig. 11 only shows analytical results based on $\psi = 0.75$ (only CCC is affected by ψ).

Table 6 Comparison of experimental and analytical results for TW4.

Result Type	DEC		SPL		LLP		CCC	
	V_{dec} (kN)	Θ_{dec} (%)	V_{spl} (kN)	Θ_{spl} (%)	V_{llp} (kN)	Θ_{llp} (%)	V_{ccc} (kN)	Θ_{ccc} (%)
Exp.(east)	134	0.04	432	0.74	588[a]	2.84[a]	463[b]	2.97[b]
Exp.(west)	143	0.05	460	0.94	625	2.90	454[b]	3.59[b]
FM[c], ψ=0.75[d]	142	0.04	500	0.59	745	2.85	611 (717)[d]	2.45 (3.50)[d]
FM[m], ψ=0.75[d]	141	0.04	416	0.52	635	2.52	696 (701)[d]	3.48 (4.66)[d]
SM, ψ=0.75[d]	132	0.04	-	-	659	2.71	659	3.14 (4.14)[d]

1 kN = 0.2248 kips.
[a]LLP was not reached (i.e., PT1 did not yield); values correspond to limit state of maximum base shear.
[b]In eastward direction, CCC was reached in 3rd cycle to 3% drift; in 1st cycle to 3% drift the maximum V was 560 kN; in westward direction, CCC was reached in 2nd cycle to 3.5% drift; in 1st cycle to 3.5% drift the maximum V was 625 kN.
[c]cyclic loading.
[d]results are for $\psi = 0.95$, except for results in parentheses which are for $\psi = 1.0$.
[m]monotonic loading.

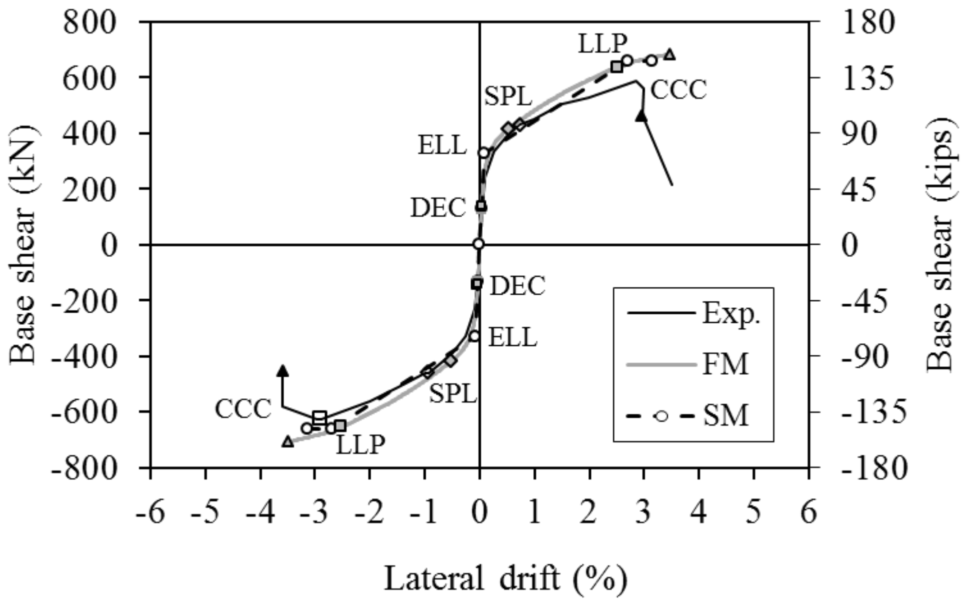

Fig. 11 Comparison of experimental envelope and analytical monotonic results (TW4)

Fig. 11 and Table 6 show that at DEC and SPL, the base shear values from both analytical models are within 12% of the experimental results. V_{llp} is overestimated by 19% using cyclic FM analysis. However, based on monotonic FM analysis, V_{llp} is overestimated by only 2% (see Fig. 11). The SM overestimates V_{llp} by about 5%. V_{ccc} is overestimated by the monotonic FM and by the SM by about 50%, because they do not account for strength loss due to cyclic loading.

The lateral drift results at DEC, Θ_{dec}, are underestimated by the FM by 11%. Θ_{llp} is underestimated by the monotonic FM by 13% and by the cyclic FM by 2%. Θ_{spl} is underestimated by the FM by about 30%. The cyclic FM with ψ = 1.0 overestimates Θ_{ccc} by less than 7%, while the monotonic FM with ψ = 0.75 overestimates Θ_{ccc} by 6%. The SM with ψ = 1.0 overestimates Θ_{ccc} by 26%, while the SM with ψ = 0.75 underestimates Θ_{ccc} by 4%.

Fig. 12 compares the cyclic experimental base shear versus lateral drift results with cyclic and monotonic loading analysis results from the fiber model (FM) for TW5. Fig. 12 shows: (1) TW5 reaches a maximum lateral drift of 6% without failing (the test was terminated because the maximum stroke of the lateral load actuator was reached); (2) the FM cyclic lateral load response consistently overestimates the experimental cyclic base shear response of TW5; (2) the FM monotonic response produces a good upper bound to the experimental cyclic response; (3) the FM cyclic response with ψ = 1.0 results in a better estimation of the lateral drift at CCC than with ψ= 0.75, although this drift is significantly underestimated; and (4) the FM monotonic response with ψ = 1.0 results in a better estimation of the lateral drift at CCC than with ψ = 0.75.

Fig. 12 shows that the cyclic FM response exceeds the monotonic FM response. As noted earlier, this occurs due to equilibrium errors in the FM resulting from overshoot tolerances that were relaxed so that the analysis could be completed[5]. Thus, this equilibrium error was observed for TW4 and TW5, both lightly-prestressed walls (see Table 1.)

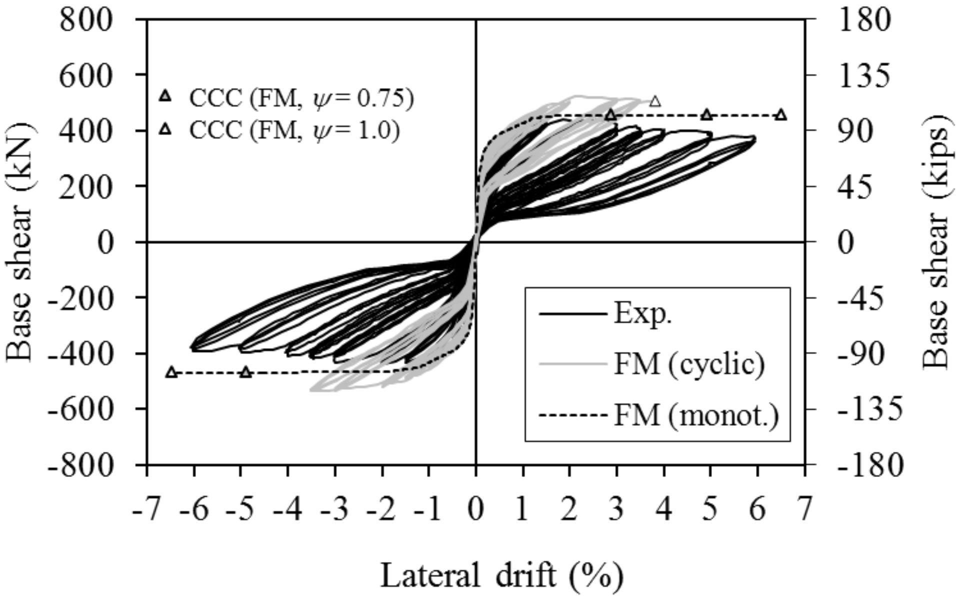

Fig. 12 Comparison of experimental and analytical results under cyclic loading (TW5)

Table 7 shows analytical and experimental base shear and lateral drift values for TW5 at specific limit states. Fig. 13 compares the experimental envelope lateral load response of TW5 to monotonic analysis results using the FM and SM. Table 7 includes analytical results for $\psi = 0.75$ and $\psi = 1.0$; however, Fig. 13 only shows analytical results based on $\psi = 0.75$ (only CCC is affected by ψ).

Table 7 Comparison of experimental and analytical results for TW5.

Result Type	DEC		SPL		LLP		CCC	
	V_{dec} (kN)	Θ_{dec} (%)	V_{spl} (kN)	Θ_{spl} (%)	V_{llp} (kN)	Θ_{llp} (%)	V_{ccc} (kN)	Θ_{ccc} (%)
Exp.(east)	126	0.05	387	0.65	435	1.44	363[a]	5.9[a]
Exp.(west)	133	0.04	382	0.65	435	1.50	375[a]	6.1[a]
FM[c], ψ=0.75[b]	151	0.04	394	0.54	472	1.27	459 (508)[b]	2.87 (3.81)[b]
FM[m], ψ=0.75[b]	148	0.04	392	0.53	447	1.19	463 (463)[b]	4.90 (6.48)[b]
SM, ψ=0.75[b]	132	0.04	-	-	443	1.26	443	4.71 (6.25)[b]

1 kN = 0.2248 kips.
[a]CCC was not reached (i.e., wall did not fail); values correspond to 3rd cycle to 6% drift, where actuator stroke limits were reached.
[b]results are for ψ = 0.95, except for results in parentheses which are for ψ = 1.0.
[c]cyclic loading.
[m]monotonic loading.

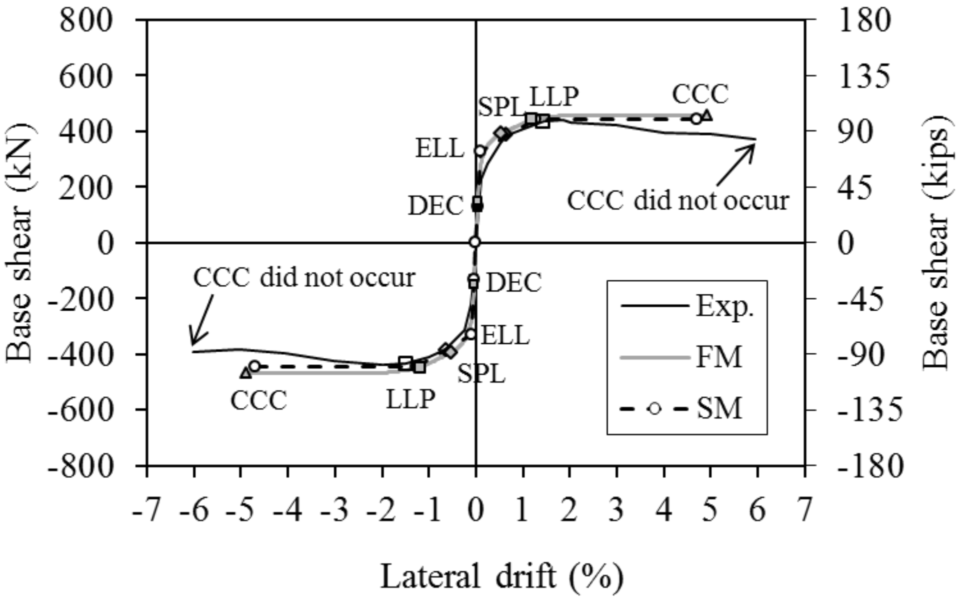

Fig. 13 Comparison of experimental envelope and analytical monotonic results (TW5)

Fig. 13 and Table 7 show that at DEC, SPL, and LLP, the base shear values from both analytical models are within 17% of the experimental results. V_{dec} and V_{llp} obtained from the SM are within 2% of the experimental results. V_{llp} is overestimated by 8% using cyclic FM analysis. However, based on monotonic FM analysis, V_{llp} is overestimated by only 3% (see Fig. 13). V_{ccc} is overestimated by the monotonic FM and by the SM by about 25%, because they do not account for strength loss due to cyclic loading. Since CCC did not occur for TW5, this comparison is based on the last recorded base shear value at a drift of 6%.

The lateral drift results at DEC, Θ_{dec}, are underestimated by the FM and SM by 11%. Θ_{llp} is underestimated by the monotonic FM by 19% and by the cyclic FM and SM by 14%. Θ_{spl} is underestimated by the FM by about 18%. The cyclic FM with ψ = 1.0 underestimates Θ_{ccc} by 37%, while the monotonic FM with ψ = 0.75 underestimates Θ_{ccc} by 18%. The monotonic FM with ψ = 1.0 provides a better estimate of Θ_{ccc}, with an 8% error. The best estimate of Θ_{ccc} is obtained from the SM with ψ = 1.0. The monotonic FM base shear results are in better agreement with experimental base shear results than are the cyclic FM base shear results for TW5. This is attributed to the relaxed overshoot tolerances required for completion of the analysis.

SUMMARY AND CONCLUSIONS

This paper compares the analytical and experimental lateral load response of five unbonded post-tensioned precast (UPT) concrete test walls, referred to as TW1 through TW5. A design-oriented analytical model is introduced, which uses simple formulae to estimate the nonlinear lateral load behavior of UPT walls. This simple model (SM) is compared with experimental results. A previously developed UPT wall model based on fiber elements (FM) is also compared with experimental results. Tests show that the limit states that characterize the lateral load response of the test walls are decompression at the wall base (DEC), initiation of cover spalling (SPL), yielding of PT steel (LLP), and crushing of confined concrete (CCC). Comparisons for TW1 under monotonic loading show good agreement between experimental and analytical base shear and lateral drift quantities using both the FM and the SM (with ψ = 0.95). Comparisons for TW2 through TW5 under cyclic loading show that the SM best estimates V_{dec}, Θ_{dec}, and Θ_{ccc} (with ψ = 0.75); the monotonic FM best estimates V_{spl} and V_{llp}; and the cyclic FM best estimates Θ_{llp}, V_{ccc} (with ψ = 0.75). The monotonic FM and the cyclic FM give similar estimates for Θ_{spl} (the SM does not consider the limit state of SPL).

The SM is found to be sufficiently accurate for seismic design of UPT walls. The accuracy of the FM in predicting the cyclic response of a UPT wall depends on the amount of initial prestress on the wall. It was observed that for lightly prestressed walls, FM cyclic results overestimate the base shear capacity obtained from the experiment, from SM analysis and from the FM monotonic analysis. It is recommended that FM monotonic analysis or analysis using the SM be carried out to verify FM cyclic analysis results.

ACKNOWLEDGMENTS

This research was conducted at the Advanced Technology for Large Structural Systems (ATLSS) Engineering Research Center at Lehigh University. The authors are grateful for funding from the National Science Foundation (Award No. 9612165), the Precast/Prestressed Concrete Institute, and the Pennsylvania Department of Community and Economic Development through a grant to the Pennsylvania Infrastructure Technology Alliance. Numerous individuals from the precast concrete industry provided assistance and materials for the experimental program. The authors thank the ATLSS

Center and Fritz Laboratory technical staff and Professor Emeritus Le-Wu Lu for their contributions. The findings, opinions, and conclusions expressed in the paper are those of the authors, and do not necessarily reflect the opinions of those acknowledged here.

REFERENCES

1. Kurama, Y.C., Sause, R., Pessiki, S., and Lu, L.-W. (2002). "Seismic Response Evaluation of Unbonded Post-Tensioned Precast Walls," *ACI Structural Journal*, V. 99, No. 5, pp. 641-651.
2. Kurama, Y. C., Sause, R., Pessiki, S., and Lu, L.-W., "Lateral Load Behavior and Seismic Design of Unbonded Post-Tensioned Precast Concrete Walls," *ACI Structural Journal*, American Concrete Institute, Vol. 96, No. 4, July-August 1999, pp. 622-632.
3. Kurama, Y.C., Pessiki, S., Sause, R., and Lu, L.-W. (1999b). "Seismic Behavior and Design of Unbonded Post-Tensioned Precast Concrete Walls," *PCI Journal*, V. 44, No. 3, pp. 72-89.
4. Perez, F.J., Pessiki, S., Sause, R., and Lu L.-W., "Lateral Load Tests of Unbonded Post-Tensioned Precast Concrete Walls," *Large-Scale Structural Testing*, ACI SP-211, 2003, pp. 161-182.
5. Perez, F.J., Pessiki, S., and Sause, R. (2004). "Experimental and Analytical Lateral Load Response of Unbonded Post-Tensioned Precast Concrete Walls," Center for Advanced Technology for Large Structural Systems (ATLSS) Report No. 04-11, Lehigh University, Bethlehem, PA.
6. Priestley, M.J.N., Sritharan, S., Conley, J.R., and Pampanin, S. (1999). "Preliminary Results and Conclusions from the PRESSS Five-Story Precast Concrete Test Building," *PCI Journal* 44(6), pp. 42-67.
7. Restrepo, J.I. and Rahman, A., "Seismic Performance of Self-Centering Structural Walls Incorporating Energy Dissipators," *Journal of Structural Engineering* V. 133, No. 11, November 2007, 1560-1570.
8. Perez, F.J., Sause, R., and Pessiki, S., "Analytical and Experimental Lateral Load Behavior of Unbonded Posttensioned Precast Concrete Walls," *Journal of Structural Engineering* V. 133, No. 11, November 2007, pp. 1531-1540.
9. Paulay, T. and Priestley, M.J.N. (1992). *Seismic Design of Reinforced Concrete and Masonry Buildings*, John Wiley & Sons, Inc.
10. Mander, J., Priestley, M., and Park, R., "Theoretical Stress-Strain Model for Confined Concrete," *Journal of Structural Engineering*, American Society of Civil Engineers, Vol. 114, No. 8, August 1988, pp. 1804-1826.
11. Oh, B., "A Plasticity Model for Confined Concrete Under Uniaxial Loading," Ph.D. Dissertation, Department of Civil and Environmental Engineering, Lehigh University, Bethlehem, PA, 2002.
12. Prakash, V., Powell, G.H., and Campbell, S. (1993). "DRAIN-2DX: Static and Dynamic Analysis of Plane Structures," NISEE, Earthquake Engineering Research Center, University of California, Berkeley, CA.
13. Horan, S. M., "Materials Modeling for Unbonded Post-Tensioned Precast Concrete Walls," M.S. Thesis, Department of Civil and Environmental Engineering, Lehigh University, Bethlehem, PA, 2002.